This is a repository copy of *The limitations of hibonite as a single-mineral oxybarometer for early solar system processes*.

White Rose Research Online URL for this paper:
http://eprints.whiterose.ac.uk/114587/

Version: Accepted Version

eprints@whiterose.ac.uk
https://eprints.whiterose.ac.uk/

1   **The limitations of hibonite as a single-mineral oxybarometer for early solar system**

2   **processes**

3

4   **Andrew J. Berry[1,2,3], Paul F. Schofield[3], Antonina N. Kravtsova[4], Laura A. Miller[2],**

5   **Natasha R. Stephen[5], Andrew M. Walker[6], Alexander V. Soldatov[4], Trevor R. Ireland[1],**

6   **K. Geraki[7], and J. Fred W. Mosselmans[7]**

7

8   [1]Research School of Earth Sciences, Australian National University, Canberra, ACT, 2601,

9   Australia

10   [2]Department of Earth Science and Engineering, Imperial College London, South Kensington,

11   SW7 2AZ, UK

12   [3]Department of Earth Sciences, Natural History Museum, Cromwell Road, London, SW7

13   5BD, UK

14   [4]International Research Centre Smart Materials, Southern Federal University, Sorge 5,

15   Rostov-on-Don, 344090, Russia

16   [5]Plymouth Electron Microscopy Centre, Plymouth University, Drake Circus, Plymouth, PL4

17   8AA, UK

18   [6]School of Earth and Environment, University of Leeds, Leeds, LS2 9JT, UK

19   [7]Diamond Light Source, Harwell Science and Innovation Campus, Didcot, OX11 0DE, UK

20

21

22   **Abstract**

23

24   The relationships between the composition of hibonite with the general formula $CaAl_{12-2x-y}Mg_xTi^{4+}_xTi^{3+}_yO_{19}$,

25   the oxidation state of Ti ($Ti^{3+}/\Sigma Ti$, where $\Sigma Ti = Ti^{3+} + Ti^{4+}$), and oxygen

26   fugacity (fO_2) were investigated experimentally.   It was found that hibonite can be

27   synthesised with a range of $Ti^{3+}/\Sigma Ti$ values at constant fO_2 and with a constant $Ti^{3+}/\Sigma Ti$ value

28   for a range of fO_2s.   It was also found that if hibonite with the formula $CaAl_{12-y}Ti^{3+}_yO_{19}$

29   ($Ti^{3+}/\Sigma Ti = 1$) is equilibrated with a melt of CAI composition at fO_2s below the iron-wüstite

30   buffer then the resulting hibonite contained Mg, with Mg per formula unit (pfu) ~ 0.8 Ti pfu,

31   and $Ti^{3+}/\Sigma Ti \sim 0.2$, irrespective of the fO_2.   These results suggest that the availability of Mg,

32   rather than fO_2, is the key factor that determines $Ti^{3+}/\Sigma Ti$ of hibonite.   The structures of

33   synthetic samples of hibonite with the general formula $CaAl_{12-2x}Mg_xTi^{4+}_xO_{19}$, where $0 \leq X <$

34   1, were determined by Rietveld refinement of X-ray powder diffraction data.   The

35   predominant site occupied by Ti^{4+} was found to change from M2 to M4 with increasing Ti

36 content. The range of Ti concentrations over which the site occupancy changed corresponds
37 to that observed in meteoritic hibonite. This change in the Ti^{4+} site produces changes in the
38 Ti K-edge XANES spectra, particularly in the intensity of the pre-edge feature, for constant
39 $Ti^{3+}/\Sigma Ti$. The observed dependence of the pre-edge on the Ti^{4+} site was reproduced by *ab*
40 *initio* simulations of the XANES spectra. The XANES spectra of natural hibonite with
41 variable Ti content from the Murchison carbonaceous chondrite closely match the spectra of
42 the synthetic samples with similar Ti contents. These differences in the spectra of meteoritic
43 hibonite could be misinterpreted as being due to changes in $Ti^{3+}/\Sigma Ti$, but are instead due to
44 differences in ΣTi, which relate to the petrogenetic history. Crystal chemistry exerts a first
45 order control on the Ti site occupancy and $Ti^{3+}/\Sigma Ti$ value of hibonite. As a result, no simple
46 relationship between $Ti^{3+}/\Sigma Ti$ and fO_2 should be expected. It is unlikely that hibonite will be
47 useful as an oxybarometer for solar processes without $Ti^{3+}/\Sigma Ti$ standards that are
48 compositionally matched to the unknown.
49
50 **Key Words**
51
52 hibonite, calcium hexaluminate, CA6, CAI, oxybarometry, solar nebula, crystal chemistry,
53 oxygen fugacity, XANES, FDMNES
54
55

2

Introduction

55

56

57 Hibonite ($CaAl_{12}O_{19}$) is the second mineral, after corundum, to condense from a gas of solar

58 composition (Kornacki and Fegley 1986; Yoneda and Grossman 1995; Lodders 2003). It

59 incorporates varying amounts of Ti as both Ti^{3+} and Ti^{4+}. Ti^{3+} substitutes directly for Al^{3+}

60 whereas Ti^{4+} undergoes a charge coupled substitution with Mg^{2+} ($Ti^{4+} + Mg^{2+} = 2Al^{3+}$). A

61 general formula for Ti-bearing hibonite is $CaAl_{12-2x-y}Mg_xTi^{4+}{}_xTi^{3+}{}_yO_{19}$. There are five Al

62 sites in hibonite (M1-M5) and their multiplicity and coordination numbers are given by

63 $^{[12]}Ca^{[6]}M1^{[5]}M2^{[4]}M3_2{}^{[6]}M4_2{}^{[6]}M5_6O_{19}$ (where coordination numbers are superscripted in

64 square brackets and the multiplicity of the site is subscripted). It has been shown recently by

65 neutron powder diffraction (NPD) of synthetic hibonite, and density functional theory (DFT),

66 that Ti^{3+} occupies adjacent face-sharing octahedral M4 sites due to a stabilising Ti-Ti

67 interaction, Ti^{4+} occupies both the M2 and M4 sites (~ 1:5 at 1400 ˚C) with the occupancy of

68 M4 again stabilised by a Ti-Ti interaction, and Mg occupies the tetrahedral M3 site and Mg-

69 Ti interactions are not important (Doyle et al. 2014). These site occupancies are broadly

70 consistent with results obtained by single-crystal X-ray diffraction (Giannini et al. 2014). In

71 dilute systems, where Ti is present as isolated cations, Ti^{3+} is predicted to occupy M2, Ti^{4+} the

72 M2 site, and Mg^{2+} the M3 site (Doyle et al. 2014).

73

74 It has been proposed that the ratio of Ti^{3+} to Ti^{4+} in hibonite, given as $Ti^{3+}/\Sigma Ti$ where $\Sigma Ti =$

75 $Ti^{3+} + Ti^{4+}$, may record the oxygen fugacity (fO_2) at the time of crystallisation/condensation

76 from the solar nebula or of a later reprocessing event (Ihinger and Stolper 1986; Beckett et al.

77 1988). The presence of Ti^{3+} results in a blue colour that is often considered to be diagnostic

78 of meteoritic hibonite and the intensity of the absorption band that gives rise to this colour has

79 been used to provide constraints on the fO_2 at which crystals equilibrated (Ihinger and Stolper

80 1986). $Ti^{3+}/\Sigma Ti$ in hibonite has been quantified from the intensity of the electron spin

81 resonance (ESR) signal arising from the unpaired electron in Ti^{3+}, and values of ~ 0.2 were

82 obtained for samples from the Murchison carbonaceous chondrite (Beckett et al. 1988),

83 however, relating $Ti^{3+}/\Sigma Ti$ to fO_2 was compromised by the uncertain Ti site occupancies.

84 These attempts to determine fO_2 using hibonite gave values that were either poorly

85 constrained or significantly more oxidised than expected.

86

87 X-ray absorption near edge structure (XANES) spectroscopy is a technique that allows

88 oxidation state ratios to be determined with micron spatial resolution and a precision of ± 1%

89 (absolute) (e.g. Berry et al. 2008, 2010). It has been used to determine the Ti site and

90 oxidation state in minerals (e.g. Berry et al. 2007; Simon et al. 2007; Tailby et al. 2011).

91 Spatially-resolved soft X-ray spectroscopies such as X-ray photo-emission electron
92 microscopy (XPEEM) and scanning transmission X-ray microscopy (STXM) also have the
93 potential to accurately quantify oxidation states and image their distribution (Schofield et al.
94 2014). Integral to correctly interpreting the results of any spectroscopic technique in terms of
95 $Ti^{3+}/\Sigma Ti$ is an understanding of the crystal chemistry, since cations with the same oxidation
96 state at different crystallographic sites can give different spectra.
97
98 Here we present the results of three sets of experiments on the roles of crystal chemistry and
99 fO_2 on the $Ti^{3+}/\Sigma Ti$ value of hibonite and hence the suitability of hibonite as a single mineral
100 oxybarometer. Firstly, the site occupied by Ti^{4+} in hibonite with the general formula $CaAl_{12-2x}Mg_xTi^{4+}_xO_{19}$
101 (i.e. $Ti^{3+}/\Sigma Ti = 0$) was determined for variable ΣTi by Rietveld refinement of
102 X-ray diffraction (XRD) data. XANES spectra of these samples were compared to those
103 predicted for Ti^{4+} at different defect sites and those of meteoritic hibonite. Secondly, hibonite
104 with the general formula $CaAl_{12-y}Ti^{3+}_yO_{19}$ (i.e. $Ti^{3+}/\Sigma Ti = 1$) was equilibrated with a melt of
105 calcium-aluminium inclusion (CAI) composition, at different fO_2s. These experiments were
106 designed to simulate possible reactions between early-formed hibonite and further condensate
107 or melt in the solar nebula. Thirdly, oxides corresponding to hibonite with the general
108 formula $CaAl_{12-2x-y}Mg_xTi^{4+}_xTi^{3+}_yO_{19}$ were equilibrated at 1400 °C to determine the fO_2 range
109 over which hibonite with a particular $Ti^{3+}/\Sigma Ti$ value can be synthesised.
110
111
112 **Experimental**
113
114 Samples are identified by reference to their Ti per formula unit (pfu) and $Ti^{3+}/\Sigma Ti$ ratios using
115 the notation (Ti pfu, $Ti^{3+}/\Sigma Ti$). For example, the sample (1.0, 1.0) will have 1.0 Ti pfu and all
116 the Ti will be Ti^{3+} giving a chemical formula of $CaAl_{11.0}Ti_{1.0}O_{19}$. The sample (1.0, 0.0) will
117 have 1.0 Ti^{4+} pfu (and 1.0 Mg^{2+} pfu) giving a chemical formula of $CaAl_{10.0}Ti_{1.0}Mg_{1.0}O_{19}$.
118
119 To investigate the effect of different amounts of Ti^{4+} on the structure of hibonite, samples
120 with the compositions (0.0, 0.0), (0.1, 0.0), (0.2, 0.0), (0.3, 0.0) and (0.4, 0.0) (i.e. the general
121 formula $CaAl_{12-2x}Mg_xTi^{4+}_xO_{19}$) were prepared from stoichiometric mixtures of $CaCO_3$, Al_2O_3,
122 $(NH_4)_2TiO(C_2O_4)_2.nH_2O$ ($n \sim 1$; ammonium titanium oxalate or ammonium
123 bis(oxalato)oxotitanate(IV) hydrate, CAS 10580-03-7) and $Mg(NO_3)_2.nH_2O$ ($n \sim 6$).
124 $(NH_4)_2TiO(C_2O_4)_2.nH_2O$ and $Mg(NO_3)_2.nH_2O$ were standardised by firing at 1000 °C to
125 determine the yields of TiO_2 and MgO, respectively. $(NH_4)_2TiO(C_2O_4)_2.nH_2O$ is soluble in

126   water, and $Mg(NO_3)_2.nH_2O$ is soluble in both water and acetone, and solutions of each were

127   added separately to a mixture of $CaCO_3$ and Al_2O_3 and stirred until the solvent evaporated.

128   The addition of Ti and Mg in solution ensures that these elements, which are present at low

129   concentrations, are homogeneously distributed in the resulting mix. The mix was pressed into

130   a pellet and heated at 1400 ˚C (the incongruent melting point of $CaAl_{12}O_{19}$ is 1852 ˚C;

131   Jerebtsov and Mikhailov 2001) in an atmosphere of CO_2 (corresponding to an fO_2 of +6.7 log

132   units relative to the iron-wüstite, IW, buffer) for 24 h, cooled to 600 ˚C, reground, and re-

133   heated at 1400 ˚C for a further 24 h. Samples of (0.44, 0.0), (0.98, 0.0), and (0.20, 1.0) were

134   prepared previously from mixtures of $CaCO_3$, Al_2O_3, TiO_2, and MgO (Doyle et al. 2014).

135

136   To investigate changes in hibonite composition due to equilibration with a melt, samples of

137   Ti^{3+} hibonite were prepared from mixtures of $CaCO_3$, Al_2O_3, and $(NH_4)_2TiO(C_2O_4)_2.nH_2O$

138   ((0.15, 1.0) and (0.25, 1.0)), or $CaCO_3$, Al_2O_3, and TiO_2 ((0.30, 1.0)), in equilibrium with

139   graphite and CO at 1400 ˚C, powdered, and mixed with either composition Hib2Ti5 of

140   Beckett and Stolper (1994) (SiO_2 21.18, TiO_2 4.85, MgO 3.35, Al_2O_3 44.53, CaO 26.55, all as

141   wt%, called A, prepared from oxides and $CaCO_3$) or a modified version of this composition

142   without TiO_2 (called B), in the proportions 40% hibonite, 60% Hib2Ti5 (by wt). The

143   composition Hib2Ti5 was chosen because it gives melt and hibonite at ~ 1450 ˚C over an fO_2

144   range from at least IW-3.3 to IW+6.6. The resulting powders were mixed with polyethylene

145   oxide and water to form a paste, which was mounted on wire loops, and equilibrated at 1450

146   ˚C and values of $\log fO_2$ corresponding to IW-0.3, -1.3, -2.3, -3.3, and -4.3. The loops were

147   made of Pt for IW-0.3, -1.3, and -2.3, and Re for IW-3.3 and -4.3. The fO_2 was controlled

148   using mixtures of CO and CO_2. Powders were also pressed into a pellet and equilibrated with

149   graphite and CO (IW-6.3). After at least 24 h the samples were quenched in water (see

150   Burnham et al. 2015 for further experimental details).

151

152   To investigate the fO_2 stability range of hibonite, mixtures of oxides corresponding to the

153   hibonite compositions (0.98, 0.0), (0.62, 0.6), and (0.33, 1.0) were pressed into pellets and

154   heated at 1400 ˚C and values of $\log fO_2$ equal to IW-6.3, -2.3, -0.3, +2.3, +4.3, +7.3, as

155   described above, for ~ 24 h. All samples were held in Pt wire baskets except for those at IW-

156   6.3, which were in graphite.

157

158   Portions of all samples were mounted in epoxy resin and polished for imaging and XANES

159   spectroscopy. Portions were also powdered for quantitative phase analysis and structural

160   characterisation using XRD. Samples of hibonite from the Murchison carbonaceous

161   chondrite (Ireland 1988, 1990) were presented as crystal fragments pressed into gold (Ireland

162   et al. 1992).

163

164   High-spatial-resolution back-scattered electron (BSE) images and elemental maps were

165   acquired using a JEOL 7001 FE-SEM, operating at 15 kV and a working distance of 10 mm,

166   with AZtec software (Oxford Instruments). Compositions were determined using a Cameca

167   SX-100 electron probe (EPMA), operating at 15 kV and 20 nA, with LTAP (for Si, Mg and

168   Al) and PET (for Ca and Ti) crystals. Wollastonite (for Si and Ca), forsterite (Mg), corundum

169   (Al) and synthetic $MnTiO_3$ (Ti) were used as standards and the detection limits (wt%) were

170   0.02 for Si, Mg and Al, 0.05 for Ca, and 0.04 for Ti.

171

172   XRD patterns were collected using a θ/2θ PANalytical X'Pert Pro α1 X-ray diffractometer

173   with an X'celerator real-time strip-detector that has an active detector length of 2.122 ˚. Data

174   for quantitative phase analysis (QPA) and structural characterisation were collected using Cu

175   Kα and Cu Kα₁ radiation, respectively. For QPA, data were collected from powdered

176   samples on kapton film, in transmission geometry, between 5 and 97 º2θ using a step size of

177   0.017 º and a scan rate of 0.001 ˚s⁻¹, resulting in total scan times of ~ 23 h. For structural

178   characterisation, data were collected from powdered samples packed into a top-loaded deep-

179   well sample holder, in reflection geometry, between 5 and 125 º2θ using a step size of 0.017 º

180   and a scan rate of 0.0056 ˚s⁻¹, resulting in total scan times of ~ 6 h. The samples were spun in

181   the plane of the sample surface during data collection in both geometries. The resulting

182   patterns were analysed by Rietveld refinement within the GSAS (General Structure Analysis

183   System) code of Larson and Von Dreele (1994) interfaced with EXPGUI (Toby 2001). For

184   both the QPA and crystal structure refinements the starting models used data for Ti-bearing

185   hibonite from Doyle et al. (2014). For the QPA, peak profiles (type 2) were modelled using

186   the model-dependent Le Bail method and the backgrounds using a six-term power series

187   function. Phases were identified by pattern matching using the JCPDS database of the

188   International Centre for Diffraction Data. Phase proportions were quantified using the

189   Rietveld method in which the scale factor, phase fractions and cell parameters were refined

190   simultaneously. The unit cell parameters were allowed to vary but no attempt was made to

191   iterate the site occupancies. The refinements were constrained to maintain chemical mass

192   balance such that the final chemistry closely matched the composition of the original oxide

193   mix. The final refinement sequences included a six-term, spherical-harmonic preferred

194   orientation parameter for hibonite. For the crystal structure refinements, peak profiles (type

195   2) were also modelled using the Le Bail method but the backgrounds used a four-term power

196   series function. The structural parameters of additional phases (if any) were added, the

197   diffraction patterns were scaled, and then all phases were refined simultaneously. For

6

198 hibonite, the unit-cell parameters were refined first, followed by the atomic coordinates and

199 atomic displacement parameters (ADP). The Ti (and Mg by stoichiometry) site occupancies

200 were fixed during the least squares refinements and manually iterated between refinement

201 cycles.

202

203 Titanium K-edge XANES spectra were recorded at I18 of Diamond Light Source

204 (Mosselmans et al. 2009). The excitation energy was selected using a Si(111)

205 monochromator and calibrated by defining the first derivative peak of a Ti foil spectrum to be

206 at 4966.4 eV. The energy resolution at the Ti K-edge was 0.70 eV, which when coupled with

207 the Ti Kα core-hole width of 0.94 eV resulted in a spectral resolution of 1.2 eV. High-energy

208 harmonics were removed by Rh coated KB mirrors that were used to focus the beam to ~ 3 x

209 3 μm. The penetration depth of Ti K-edge X-rays (absorption length) in $CaAl_{12}O_{19}$ is ~ 17

210 μm. Fluorescence was detected using either a nine-element Ge or a four-element Si drift

211 (Vortex) detector and the distance between the detector and sample was adjusted to ensure

212 that the total incoming count rate was within the linear range of the signal processing

213 electronics. Samples were mounted at 45° to both the incident beam and the detector. Spectra

214 were recorded from 4950-5200 eV with a step size of 0.5 eV for the baseline (4950-4960 eV),

215 0.1 eV for the pre-edge (4960-4975), 0.2 eV for the edge (4975-5015) and 2.5 eV above the

216 edge. The total spectral acquisition time was ~ 20 min. The Ti Kα fluorescence intensity was

217 dead-time corrected, normalised to the intensity of the incident beam, and the resulting

218 spectra compared after subtraction of a constant baseline and normalisation to the average

219 intensity above 5145 eV. For the synthetic samples spectra were recorded from a number of

220 points. Spectra of meteoritic crystals were recorded for random orientations.

221

222 The Ti K-edge XANES spectra of Ti^{3+} and Ti^{4+} occupying various sites in hibonite were

223 simulated using the full-potential finite difference method to solve the Schrödinger equation

224 in real space while accounting for the core hole created by the electronic transition. The

225 simulations made use of the FDMNES program (Joly 2001, Bunau and Joly 2009) and the

226 Hedin-Lundquist exchange-correlation potential. Atomic geometries corresponding to the

227 different defects used in the simulations were taken from the DFT calculations described in

228 Doyle et al. (2014). Specifically, spectra were calculated for isolated Ti^{3+} on M2, isolated

229 Ti^{4+} on either M2 or M4, and clusters of either two Ti^{3+} or two Ti^{4+} on adjacent face-sharing

230 M4 sites. Ti^{4+} was charge balanced by Mg^{2+} on M3. These geometries correspond to models

231 $Ti_{Al(2)}^{\times}$, $\{Ti_{Al(2)}^{\bullet}Mg_{Al(3)}'\}_b$, $\{Ti_{Al(4)}^{\bullet}Mg_{Al(3)}'\}$, $\{Ti_{Al(4)}^{\times}Ti_{Al(4)}^{\times}\}$ and

232 $\{Ti_{Al(4)}^{\bullet}Ti_{Al(4)}^{\bullet}Mg_{Al(3)}'Mg_{Al(3)}'\}$, respectively, in Tables 5 and 6 of Doyle et al. (2014). For

233 each model a spherical atomic cluster of radius 5.6 Å around the central Ti cation was

7

234 extracted from the periodic model (previously subjected to geometry optimisation using DFT)

235 and this finite cluster was used for the simulation of the XANES spectra. The calculated

236 spectra were arbitrarily shifted in energy in order to align them with the experimental spectra.

237

238

239   **Results**

240

241 The $CaAl_{12-2x}Mg_xTi^{4+}_xO_{19}$ samples (i.e. those prepared at 1400 ˚C and IW+6.7) were white,

242 polycrystalline aggregates (crystals ~ 5 μm), and were either phase pure within the detection

243 limits of XRD or contained traces (< 2 wt%) of Al_2O_3. The lattice parameters and site

244 occupancies determined by Rietveld refinement of the XRD data are given in Table 1. This

245 includes new data for samples (0.44, 0.0) and (0.98, 0.0) for which the structures have been

246 determined previously using NPD data (Doyle et al. 2014). The dependencies of the *c* lattice

247 parameter and unit cell volume on Ti content for these samples, and determined by NPD

248 (Doyle et al. 2014) and X-ray single-crystal diffraction (Giannini et al. 2014) for samples with

249 a range of $Ti^{3+}/\Sigma Ti$ values, are shown in Figure 1. The *a* lattice parameter (not plotted)

250 exhibits a similarly good correlation with Ti pfu. Ti was found to only occupy the M2 and

251 M4 sites in agreement with previous studies (Doyle et al. 2014, Giannini et al. 2014). There

252 is one M2 site, which is split into two symmetrically equivalent half-occupied sites by the

253 static displacement of the M2 cation from the site-centre, and two M4 sites pfu. Therefore, Ti

254 pfu due to M2 and M4 is equal to twice the occupancy (as presented in Table 1) and M2/M4

255 in terms of occupancy is equivalent to M2/M4 in pfu. The Ti^{4+} M4 site occupancy was either

256 determined directly (for samples in which all Ti is assumed to be Ti^{4+}) or calculated by

257 assuming that the total Ti^{4+} pfu is equal to Mg^{2+} pfu and all Ti on M2 is Ti^{4+} (Doyle et al.

258 2014). Ti^{4+} on the M4 site pfu and the Ti^{4+} M2/M4 site occupancy ratio, as a function of Ti^{4+}

259 pfu, are shown in Figure 2.

260

261 All the hibonite-melt samples were blue. BSE images and elemental maps for representative

262 samples are shown in Figure 3. The BSE images of all samples show two types of euhedral

263 crystals: blocky crystals (5-15 μm), which often exhibit hexagonal symmetry and are clearly

264 zoned (rims ~ 1 μm), and elongate or lathe-like crystals (3-5 μm). The lathes and the rims of

265 the zoned crystals are similar in the BSE images and are enriched in Ti and Mg relative to the

266 cores (Fig. 3b). The correlation between the BSE images and the elemental maps suggests

267 that the zoning is real and not an edge effect. The elemental maps also show that hibonite

268 crystals that were originally Mg-free ($CaAl_{12-y}Ti^{3+}_yO_{19}$) contain significant Mg after

269   equilibration with the melt; the distribution of Al distinguishes hibonite from melt (Fig. 3d),
270   Ti is enriched in the crystals relative to what was initially a Ti-free melt (Fig. 3e), and Mg is
271   almost uniformly distributed between hibonite and melt (Fig. 3f). The compositions of the
272   crystals determined by EPMA are given in Table 2. The size of the crystals makes it difficult
273   to obtain analyses that do not contain a contribution from the surrounding quenched melt. In
274   many cases analyses were obtained for a series of points traversing a crystal in the hope of
275   identifying a point for which the melt contribution was minimal. The Si content was used as
276   an indicator of melt since hibonite contains a small or negligible amount (Beckett and Stolper
277   1994) whereas the melt contains over 20 wt% SiO_2. An example traverse is shown in Figure
278   4 where the Si content reaches a minimum value in the centre of a crystal. For many samples
279   it was not possible to obtain analyses of hibonite that were not contaminated by the melt and
280   only the analysis with the lowest SiO_2 value, if also less than 1.0 wt% (average ~ 0.4 wt%), is
281   reported in Table 2. Thus, these results are for the subset of samples for which the analyses
282   are considered reliable. For some samples two different hibonite compositions were obtained
283   and both are given in Table 2. The SiO_2 contents are consistent with values reported
284   previously for hibonite (Beckett and Stolper 1994; Simon et al. 1997), but if they were to
285   arise from the surrounding melt the associated contribution to the Mg and Ti contents of the
286   hibonite would be less than 0.1 wt%. The independence of the Si and Mg concentrations
287   shown in Figure 4 indicates that the Mg in the crystal is not an artefact attributable to the
288   melt.

289

290   The oxide compositions corresponding to (0.98, 0.0), (0.62, 0.6), and (0.33, 1.0) produced
291   polycrystalline hibonite at 1400 ˚C and all values of fO_2 (IW-6.3 to IW+7.3), plus varying
292   amounts of $CaTiO_3$, $MgAl_2O_4$, Al_2O_3, Al_2TiO_5, and Ti-oxides. The hibonite lattice
293   parameters and the phase proportions of each sample are given in Table 3, and the variations
294   of the c lattice parameter and wt% of hibonite as a function of fO_2 are shown in Figure 5. It is
295   not possible to distinguish Mg from Al using XRD data and hence site occupancies and
296    $Ti^{3+}/\Sigma Ti$ could not be determined for these samples. The powdered products were a shade of
297   blue for all three compositions at fO_2s equal to and below IW+4.3, while the product of
298   composition (0.62, 0.6) was also blue at IW+7.3.

299

300   Ti K-edge XANES spectra recorded from different points on each $CaAl_{12-2x}Mg_xTi^{4+}_xO_{19}$
301   sample were essentially identical. Spectra recorded from a randomly oriented single crystal
302   as a function of orientation to the X-ray beam were also essentially identical (Doyle et al.
303   2016). Spectra for samples (0.1, 0.0) and (0.44, 0.0) are shown in Figure 6(b, d). Also shown
304   are spectra for two hibonite crystals from the Murchison carbonaceous chondrite (10-43 and

305 7-981), which are typical of two spectral types that were observed for a number of crystal

306 fragments. Sample 10-43 (Blue AGregate or BAG) contains 6.44 wt% TiO_2 (0.55 Ti pfu) and

307 has the formula $Ca_{1.03}Al_{10.93}Mg_{0.48}Ti_{0.55}O_{19}$, while 7-981 (PLAty Crystal or PLAC) contains

308 1.19 wt% TiO_2 (0.1 Ti pfu) and corresponds to $Ca_{1.01}Al_{11.78}Mg_{0.12}Ti_{0.10}O_{19}$ (Ireland 1988).

309 The pre-edge region for these two samples, for synthetic samples with $Ti^{3+}/\Sigma Ti = 0$ but

310 varying Ti pfu, and a synthetic sample with $Ti^{3+}/\Sigma Ti =1$ (Doyle et al. 2016) are shown in

311 Figure 7. Spectra of other Murchison crystals, and hibonite in CAIs from various R3, CR2,

312 and unique meteorites will be presented elsewhere.

313

314 Ti K-edge XANES spectra for hibonite with Ti^{3+} and Ti^{4+} at various substitutional sites,

315 modelled using FDMNES, are shown in Figure 8. The pre-edge regions of the Ti^{4+} models

316 are shown in Figure 9 along with the spectrum of sample 10-43. In both figures the spectrum

317 resulting from a linear combination of the spectra for Ti^{4+} on M2 and Ti^{4+} clustered on M4, in

318 a proportion similar to that predicted by XRD and NPD for hibonite with a Ti pfu comparable

319 to that of 10-43, is also shown.

320

321

322   **Discussion**

323

324 Hibonite containing only Ti^{4+} is colourless (appears white), that containing only Ti^{3+} is grey

325 or blue, while mixed valent samples containing both Ti^{3+} and Ti^{4+} are deep blue. The blue

326 colour arises from the d^1 electronic configuration of Ti^{3+} and may correspond to either a *d-d*

327 transition or charge transfer between Ti^{3+} and Ti^{4+}, noting that such an interaction has been

328 reported for Ti in Al_2O_3 (Yamaga et al. 1994) and that Ti^{3+} and Ti^{4+} may occupy

329 neighbouring, face-sharing M4 octahedra in hibonite. The colour blue is considered to be

330 diagnostic of hibonite in CAIs (Ireland 1988) and the presence of Ti^{3+} is generally taken to

331 imply that crystals formed or equilibrated under reduced conditions.

332

333 $Ti^{3+}/\Sigma Ti$ in a melt will have a sigmoidal dependence on fO_2 (see Berry and O'Neill 2004). If

334 hibonite crystallises from a condensate (a low density melt) then $Ti^{3+}/\Sigma Ti$ in hibonite should

335 be related to $Ti^{3+}/\Sigma Ti$ in the condensate. However, the partition coefficients of Ti^{3+} and Ti^{4+}

336 will be different and the uptake of Ti^{4+} will depend on the availability of Mg (for charge

337 balance). In the absence of Mg all Ti in hibonite must be Ti^{3+} (i.e. $Ti^{3+}/\Sigma Ti = 1$), irrespective

338 of the fO_2, and the amount of Ti will depend on the activity of Ti^{3+} in the condensate or melt.

339 In the synthesis of mixed-valent samples from oxides a range of $Ti^{3+}/\Sigma Ti$ values (= 0.27, 0.33,

340 0.39. 0.60, and 1.0) were all prepared at constant fO_2 (IW-6.3) by varying the amount of Mg

341 (Doyle et al. 2014). The Mg pfu required a stoichiometric amount of Ti to be Ti^{4+} with any Ti

342 pfu > Mg pfu attributed to Ti^{3+}. Determining $Ti^{3+}/\Sigma Ti$ in these samples would thus provide no

343 insight into the fO_2 of formation.

344

345 The role of crystal chemistry was investigated further in this study by the experiments in

346 which oxide compositions corresponding to hibonites containing only Ti^{3+}, only Ti^{4+}, and

347 both Ti^{3+} and Ti^{4+} were heated at 1400 ˚C and values of fO_2 corresponding to IW-6.3 to +7.3.

348 For each composition the lattice parameters of the hibonite were similar at all fO_2s (Fig. 5a),

349 despite the sensitivity of the parameters to ΣTi (Fig. 1) and Ti^{4+} pfu (Doyle et al. 2014).

350 Although the Ti^{3+} composition yielded a large proportion of impurity phases at all fO_2s other

351 than the most reduced, hibonite was always the dominant phase for the other two

352 compositions (Fig. 5b; Table 3). Indeed, the mixed valent composition produced almost

353 phase pure hibonite over the entire fO_2 range with very little change in the lattice parameter

354 i.e. hibonite with $Ti^{3+}/\Sigma Ti = 0.6$ was prepared over 13 log units in fO_2. This suggests that

355 crystal chemistry stabilises Ti^{3+} and Ti^{4+} to significantly more oxidised and reduced

356 conditions, respectively, than might be expected. Thus, a range of $Ti^{3+}/\Sigma Ti$ values can be

357 produced at a single fO_2 and a constant $Ti^{3+}/\Sigma Ti$ value can be produced for a range of fO_2s.

358

359 Melt composition A at 1450 ˚C should produce hibonite and melt (Beckett and Stolper 1994).

360 Therefore, the equilibration experiments between hibonite and melt A might be expected to

361 yield two generations of hibonite: the pre-synthesised starting material after equilibration with

362 the melt and liquidus crystals. Melt composition B (Ti-free) was chosen to suppress the

363 formation of liquidus hibonite. The large blocky crystals are attributed to the pre-synthesised

364 hibonite and the small lathe-like crystals and rims on the blocky crystals to hibonite that

365 crystallised from the melt, either at the experimental conditions or on quenching. All

366 experiments produced both generations of hibonite, including those with melt B, indicating

367 that the pre-synthesised hibonite partially dissolved in melt B to produce a modified melt that

368 crystallised new hibonite. This is consistent with the presence of Ti in the quenched melts.

369 The composition of the pre-synthesised hibonite was of the form $CaAl_{12-y}Ti^{3+}_yO_{19}$ yet all the

370 hibonite analyses in Table 2 contain Mg in an amount approximately equal to that of Ti, in

371 pfu. The Mg, as illustrated in Figure 4, is unambiguously present in the hibonite and can not

372 be attributed to fluorescence derived from the surrounding melt. The presence of Mg,

373 seemingly homogeneously distributed in the crystals, is shown in Figure 3f. For some

374 samples different hibonite compositions are reported in Table 2 and these are attributed to the

375 re-equilibrated and liquidus crystals, however, all have Ti pfu ~ Mg pfu. The Ti pfu in some

376 cases corresponds closely to that of the pre-synthesised hibonite. In other cases the crystal

377 analysed could have grown from the melt or represent a composition closer to crystal-melt

378 equilibrium. The key point is hibonite crystals that contained Ti only as Ti^{3+} have

379 incorporated Mg during equilibration with a melt and as a result now contain Ti as

380 predominantly Ti^{4+}, at all fO_2s. The average value of $Ti^{3+}/\Sigma Ti$ calculated from stoichiometry

381 is 0.09(8), assuming Ti^{4+} pfu = Mg pfu, or 0.30(11) if Ti^{4+} + Si pfu = Mg pfu (Mg^{2+} may be

382 charge balanced by both Ti^{4+} and Si^{4+}; Simon et al. 1997). The correlation between Mg and

383 Ti + Si pfu is shown in Figure 10 and has a slope of ~ 0.8. If Ti pfu is converted to Ti^{4+} pfu

384 using the average value of $Ti^{3+}/\Sigma Ti$ then the slope of the correlation is ~ 1. The ratio of Mg to

385 Ti + Si is constant and independent of fO_2. The correlation between Mg and Ti also has a

386 slope of ~ 0.8 but does not pass through 0 (intercept 0.02). Equilibration of hibonite with a

387 melt of CAI composition results in the uptake of Mg and, for charge balance, a stoichiometric

388 amount of Ti^{3+} must be oxidised to Ti^{4+}, even at IW-6.3. This suggests that the Mg activity of

389 the melt, and hence crystal chemistry, is more important for determining the $Ti^{3+}/\Sigma Ti$ value of

390 hibonite than fO_2. These experiments were designed to simulate the equilibration of

391 crystallised/condensed hibonite with further condensate or melt and it is noted that the

392 $Ti^{3+}/\Sigma Ti$ values obtained are similar to those estimated for hibonite from the Murchison

393 carbonaceous chondrite (0.15-0.28; Beckett et al. 1988).

394

395 The condensation temperatures of the major elements, for a gas of solar composition at a

396 pressure of less than 0.01 atm, decrease in the order Al, Ca, Ti, Si, Mg, Fe (Lodders 2003).

397 Corundum is the first phase to condense (Yoneda and Grossman 1995) and may contain up to

398 0.25 wt% Ti (Simon et al. 2002), most likely as Ti^{3+}. With continued cooling and

399 condensation corundum is believed to react with Ca to form hibonite. Accordingly,

400 corundum-bearing CAIs are rare and corundum has been found enclosed by hibonite (Simon

401 et al. 2002; Nakamura et al. 2007). The first meteoritic hibonite to condense might be

402 expected to have the composition $CaAl_{12-y}Ti_yO_{19}$. Further condensation would make Mg

403 available to the system. If Mg was to equilibrate with hibonite, which at that point would

404 contain Ti as only Ti^{3+}, then Ti^{3+} must oxidise to Ti^{4+} in order for the Mg to be

405 accommodated. If new hibonite that contains Mg was to crystallise then it must also contain

406 Ti^{4+}. The addition of Mg and Ti from a melt to early-formed meteoritic hibonite has been

407 proposed as a mechanism for producing rims of secondary hibonite with different Mg:Ti

408 ratios and colours (Simon et al. 1997). Meteoritic hibonite with small blue cores surrounded

409 by thick colourless rims have been observed (Rout and Bischoff 2008). The difference in

410   colour was attributed to differences in the Ti content but could also be due to differences in

411   Mg content and hence Ti oxidation state, noting a strong 1:1 correlation between Mg pfu and

412   Ti pfu overall but Ti > Mg for the blue components. This 1:1 correlation, which is a general

413   characteristic of meteoritic hibonite (see Doyle et al. 2014), the ability to synthesise hibonite

414   under reduced conditions with almost any $Ti^{3+}/\Sigma Ti$ depending on the available Mg, and the

415   fact that hibonite with $Ti^{3+}/\Sigma Ti = 1$ will gain Mg during equilibration with a CAI melt

416   composition resulting in $Ti^{3+}/\Sigma Ti \sim 0.2$, independently of fO_2 (at least below IW), indicate

417   that stoichiometry, or the activity of Mg, is more important for controlling $Ti^{3+}/\Sigma Ti$ than fO_2.

418

419   The lattice parameters and unit cell volumes determined by X-ray powder diffraction (Table

420   1) are consistent with those of other studies (Fig. 1). The increase with Ti pfu is mainly due

421   to the corresponding increase in Mg pfu and the larger size of Mg^{2+} relative to Al^{3+} (Doyle et

422   al. 2014). XRD provides excellent contrast between Al and Ti and the occupancies of Ti^{4+} on

423   M4 (Fig. 2a) as a function of Ti^{4+} pfu are similar to those determined by NPD and single-

424   crystal XRD (Doyle et al. 2014; Giannini et al. 2014). The slope of the correlation is less than

425   1 (~ 0.8) because Ti^{4+} also occupies the M2 site. The ratio of the Ti^{4+} occupancy of M2 and

426   M4 (Fig. 2b) determined in this study varies systematically with Ti^{4+} pfu.   At low

427   concentrations Ti^{4+} predominantly occupies the M2 site, as predicted by DFT for isolated

428   cations, while at higher concentrations Ti^{4+} prefers the M4 site due to the stabilising Ti-Ti

429   interaction that occurs if adjacent M4 sites are occupied (Doyle et al. 2014). All the data are

430   in general agreement with the trend, although the mixed-valent sample with the highest value

431   of $Ti^{3+}/\Sigma Ti$ (0.62, 0.60) has an unexpectedly low Ti^{4+} M2/M4 value, which may indicate a

432   stabilising Ti^{3+}(M4)-Ti^{4+}(M4) interaction that results in Ti^{4+} occupying M4 even at low Ti^{4+}

433   pfu.

434

435   The Ti K-edge XANES spectra of the (0.1, 0.0) and (0.44, 0.0) synthetic samples are very

436   similar (pre-edge, edge, and post-edge) to those of natural samples 7-981 (0.1 Ti pfu) and 10-

437   43 (0.55 Ti pfu), respectively (Fig. 6). This is shown in more detail for the pre-edge in Figure

438   7. For the samples with $Ti^{3+}/\Sigma Ti = 0$ the pre-edge systematically decreases in maximum

439   intensity and broadens (develops shoulders at lower and higher energies) with increasing Ti^{4+}

440   pfu (from ~ 0.1 to 1.0). Over this range Ti^{4+} changes site from M2 to predominantly M4. The

441   pre-edge feature corresponds to the 1s→3d transition, which is forbidden in octahedral

442   coordination, but may gain intensity by orbital mixing in lower symmetry environments.

443   Accordingly, for Ti^{4+}, the pre-edge intensity has been shown to increase from [6]Ti to [5]Ti to

444   [4]Ti coordination (Farges et al. 1996). In hibonite a change in site symmetry from trigonal

445 bipyramidal ($^{[5]}$M2) to octahedral ($^{[6]}$M4) should therefore be associated with a decrease in

446 pre-edge intensity, as observed. The pre-edge region of 7-981 is consistent with most of the

447 Ti^{4+} occupying the M2 site (compare b and c in Fig. 7) and that of 10-43 with Ti^{4+} occupying

448 both M2 and M4 (compare a and f in Fig. 7). The effect of what would be a small (from

449 stoichiometry) amount of Ti^{3+} in 10-43 on the pre-edge is insignificant given the shape of the

450 pre-edge for (0.2, 1.0) shown in Figure 7h. Changes in Ti^{4+} site occupancy with changes in

451 concentration, at constant fO_2, produce changes in the XANES spectra that could easily be

452 misinterpreted as being due to changes in $Ti^{3+}/\Sigma Ti$. The XANES spectra of meteoritic

453 hibonite differ with ΣTi, which relates to the petrogenetic history, and the effect of differences

454 in Ti site occupancy will be convolved with any differences in $Ti^{3+}/\Sigma Ti$.

455

456 The large effect of the Ti^{4+} site occupancy on the pre-edge is confirmed by the XANES

457 models shown in Figure 9. The pre-edge for Ti^{4+} on M2 is significantly more intense, and

458 less structured than that for Ti^{4+} on M4, either as an isolated cation or as a cluster. The Ti^{4+}

459 site occupancy of sample 10-43 is expected to be around 20% M2 and 80% M4 and the

460 simulated spectrum for this occupancy is in reasonable agreement with what is observed

461 (compare a and b in Fig. 9). The agreement between the simulated and experimental spectra

462 for the edge and post-edge regions (Figs. 6 and 8) is less good but not unreasonable given the

463 complexity of the models.

464

465 To determine $Ti^{3+}/\Sigma Ti$ in hibonite by XANES spectroscopy would require a large set of well-

466 characterised standards. These standards would need to encompass not only variable $Ti^{3+}/\Sigma Ti$

467 but also different ΣTi to account for changes in the Ti site at constant $Ti^{3+}/\Sigma Ti$ and the

468 diversity of possible Ti-Ti interactions (Ti^{3+}-Ti^{3+}, Ti^{4+}-Ti^{4+}, Ti^{3+}-Ti^{4+}) across the shared face

469 of the M4 octahedra. Standards may be characterised by determining ΣTi and Mg by EPMA

470 and estimating $Ti^{3+}/\Sigma Ti$ by assuming $Ti^{4+} = Mg^{2+}$. EPMA may similarly be used to evaluate

471 $Ti^{3+}/\Sigma Ti$ of meteoritic hibonite if the amount of Si is determined accurately (Simon et al.

472 1997), although the presence of relatively small amounts of other transition metals may

473 introduce significant uncertainties.

474

475 We have shown that hibonite with almost any value of $Ti^{3+}/\Sigma Ti$ can be prepared at constant

476 fO_2 and that a constant value of $Ti^{3+}/\Sigma Ti$ can be produced over a range of fO_2. Hibonite will

477 equilibrate with a melt that contains Mg to produce a $Ti^{3+}/\Sigma Ti$ value that is independent of

478 fO_2. Meteoritic hibonite may re-equilibrate with post-formation conditions by changing its

479 Mg content and hence $Ti^{3+}/\Sigma Ti$ value. The primary factor that controls the $Ti^{3+}/\Sigma Ti$ ratio is

480 the availability of Mg rather than fO$_2$. The crystal chemistry also determines the Ti site

481 occupancy, which varies with Ti concentration. The site occupied by Ti clearly affects the

482 XANES spectrum and the potential for it to be used to determine Ti^{3+}/ΣTi. Changes in site

483 occupancy and the resulting Ti-Ti interactions will similarly affect other spectroscopic

484 techniques, such as optical absorption, ESR, XPEEM, STXM and electron energy loss

485 (EELS). The crystal chemistry of hibonite severely compromises its ability to record a

486 Ti^{3+}/ΣTi value that relates to fO$_2$ or for Ti^{3+}/ΣTi to be quantified accurately.

487

488

500

501

502 **References**

503

504 Beckett, J.R., Live, D., Tsay, F.-D., Grossman, L. and Stolper, E. (1988) Ti^{3+} in meteoritic

505 and synthetic hibonite. Geochimica et Cosmochimica Acta, 52, 1479-1495.

506

507 Beckett, J.R. and Stolper, E. (1994) The stability of hibonite, melilite and other aluminous

508 phases in silicate melts: implications for the origin of hibonite-bearing inclusions from

509 carbonaceous chondrites. Meteoritics, 29, 41-65.

510

511 Berry, A.J., O'Neill, H.St.C. (2004) A XANES determination of the oxidation state of

512 chromium in silicate glasses. American Mineralogist 89, 790-798.

513

514 Berry, A.J., Walker, A.M., Hermann, J., O'Neill, H.St.C., Foran, G.J., and Gale, J.D. (2007)

515 Titanium substitution mechanisms in forsterite. Chemical Geology, 242, 176-186.

516

517 Berry, A.J., Danyushevsky, L.V., O'Neill, H.St.C., Newville, M., and Sutton, S.R. (2008) The

518 oxidation state of iron in komatiitic melt inclusions indicates hot Archaean mantle. Nature,

519 455, 960-963.

520

521 Berry, A.J., Yaxley, G.M., Woodland, A.B., and Foran, G.J. (2010) A XANES calibration for

522 determining the oxidation state of iron in mantle garnet. Chemical Geology, 278, 31-37.

523

524 Burnham, A.D., Berry, A.J., Halse, H.R., Schofield, P.F., Cibin, G., and Mosselmans, J.F.W.

525 (2015) The oxidation state of europium in silicate melts as a function of oxygen fugacity,

526 composition and temperature. Chemical Geology, 411, 248-259.

527

528 Bunau, O. and Joly, Y. (2009) Self-consistent aspects of x-ray absorption calculations.

529 Journal of Physics: Condensed Matter, 21, 345501.

530

531 Doyle, P.M., Schofield, P.F., Berry, A.J., Walker, A.M., and Knight, K.S. (2014) Substitution

532 of Ti^{3+} and Ti^{4+} in hibonite ($CaAl_{12}O_{19}$). American Mineralogist, 99, 1369-1382.

533

534 Doyle, P.M., Berry, A.J., Schofield, P.F., and Mosselmans, J.F.W. (2016) The effect of site

535 geometry, Ti content and Ti oxidation state on the Ti K-edge XANES spectrum of synthetic

536 hibonite. Geochimica et Cosmochimica Acta, 187, 294-310.

537

538 Farges, F., Brown Jr., G.E., and Rehr, J.J. (1996) Coordination chemistry of Ti(IV) in silicate

539 glasses and melts: I. XAFS study of titanium coordination in oxide model compounds.

540 Geochimica et Cosmochimica Acta 60, 3023-3038.

541

542 Giannini, M., Boffa Ballaran, T., and Langenhorst, F. (2014) Crystal chemistry of synthetic

543 Ti-Mg-bearing hibonites: a single-crystal X-ray study. American Mineralogist, 99, 2060-

544 2067.

545

546 Ihinger, P.D. and Stolper, E. (1986) The color of meteoritic hibonite: an indicator of oxygen

547 fugacity. Earth and Planetary Science Letters, 78, 67-79.

548

549 Ireland, T.R. (1988) Correlated morphological, chemical, and isotopic characteristics of

550 hibonites from the Murchison carbonaceous chondrite. Geochimica et Cosmochimica Acta,

551 52, 2827-2839.

16

552

553 Ireland, T.R. (1990) Presolar isotopic and chemical signatures in hibonite-bearing refractory

554 inclusions from the Murchison carbonaceous chondrite. Geochimica et Cosmochimica Acta,

555 54, 3219-3237.

556

557 Ireland, T.R., Zinner, E.K., Fahey, A.J., and Esat, T.M. (1992) Evidence for distillation in the

558 formation of HAL and related hibonite inclusions. Geochimica et Cosmochimica Acta, 56,

559 2503-2520.

560

561 Jerebtsov, D.A. and Mikhailov, G.G. (2001) Phase diagram of $CaO-Al_2O_3$ system. Ceramics

562 International, 27, 25-28.

563

564 Joly, Y. (2001) X-ray absorption near edge structure calculations beyond the muffin-tin

565 approximation. Physical Review B, 63, 125120.

566

567 Kornacki, A.S. and Fegley, B. Jr. (1986) The abundance and relative volatility of refractory

568 trace elements in Allende Ca,Al-rich inclusions: implications for chemical and physical

569 processes in the solar nebula. Earth and Planetary Science Letters, 79, 217-234.

570

571 Larson, A.C. and Von Dreele, R.B. (1994) General Structure Analysis System (GSAS), Los

572 Alamos National Laboratory Report. LAUR 86-748 (revised version).

573

574 Lodders, K. (2003) Solar System abundances and condensation temperatures of the elements.

575 Astrophysical Journal, 591, 1220-1247.

576

577 Mosselmans, J.F., Quinn, P.D., Dent, A.J., Cavill, S.A., Moreno, S.D., Peach, A., Leicester,

578 P.J., Keylock, S.J., Gregory, S.R., Atkinson, K.D., and Rosell, J.R. (2009) I18 - the

579 microfocus spectroscopy beamline at the Diamond Light Source. Journal of Synchrotron

580 Radiation, 16, 818-824.

581

582 Nakamura, T.M., Sugiura, N., Kimura, A., Miyazaki, A, and Krot, A.N. (2007) Condensation

583 and aggregation of solar corundum and corundum-hibonite grains. Meteoritics and Planetary

584 Science, 42, 1249-1265.

585

586 Rout, S. and Bischoff, A. (2008) Ca,Al-rich inclusions in Rumuruti (R) chondrites.

587 Meteoritics and Planetary Science, 43, 1439-1464.

588

589   Schofield, P.F., Smith, A.D., Scholl, A., Doran, A., Covey-Crump, S.J., Young, A.T., and

590   Ohldag, H. (2014) Chemical and oxidation-state imaging of mineralogical intergrowths: The

591   application of X-ray Photo-Emission Electron Microscopy (XPEEM). Coordination

592   Chemistry Reviews, 277-278, 31-43.

593

594   Simon, S.B., Grossman, L., and Davis, A.M. (1997) Multiple generations of hibonite in

595   spinel-hibonite inclusions from Murchison. Meteoritics and Planetary Science, 32, 259-269.

596

597   Simon, S.B., Davis, A.M., Grossman, L., and McKeegan, K.D. (2002) A hibonite-corundum

598   inclusion from Murchison: a first-generation condensate from the solar nebula. Meteoritics

599   and Planetary Science, 37, 533-548.

600

601   Simon, S.B., Sutton, S.R., and Grossman, L. (2007) Valence of titanium and vanadium in

602   pyroxene in refractory inclusion interiors and rims. Geochimica et Cosmochimica Acta, 71,

603   3098-3118.

604

605   Tailby, N.D., Walker, A.M., Berry, A.J., Hermann, J., Evans, K.A., Mavrogenes, J.A.,

606   O'Neill, H.St.C., Rodina, I.S., Soldatov, A.V., Rubatto, D., and Sutton, S.R. (2011) Ti site

607   occupancy in zircon. Geochimica et Cosmochimica Acta, 75, 905-921.

608

609   Toby, B.H. (2001) EXPGUI, a graphical user interface for GSAS. Journal of Applied

610   Crystallography, 34, 210-221.

611

612   Yamaga, M., Yosida, T., Hara, S., Kodama, N., and Henderson, B. (1994) Optical and

613   electron spin resonance spectroscopy of Ti^{3+} and Ti^{4+} in Al_2O_3. Journal of Applied Physics,

614   75, 1111–1117.

615

616   Yoneda, S. and Grossman, L. (1995) Condensation of CaO-MgO-Al_2O_3-SiO_2 liquids from

617   cosmic gases. Geochimica et Cosmochimica Acta, 59, 3413-3444.

618

619

620   **Figure Captions**

621

622   Figure 1: (a) c lattice parameter and (b) V, unit cell volume, as a function of Ti pfu,

623   determined for synthetic hibonite ($CaAl_{12-2x}Mg_xTi^{4+}_xO_{19}$) in this study (circles), and from

18

624 Doyle et al. 2014 (squares) and Giannini et al. 2014 (triangles). Samples with $Ti^{3+}/\Sigma Ti = 0$

625 are denoted by solid symbols and those containing Ti^{3+} by open symbols. Error bars are

626 smaller than the symbols.

627

628 Figure 2: Ti^{4+} on (a) M4 in pfu and (b) M2/M4, as a function of Ti^{4+} pfu for synthetic hibonite

629 in this study (circles), Doyle et al. 2014 (squares), and Giannini et al. 2014 (triangles).

630 Samples with $Ti^{3+}/\Sigma Ti = 0$ are denoted by solid symbols and those containing Ti^{3+} by open

631 symbols. The error bars are smaller than the symbols except where shown.

632

633 Figure 3: FE-SEM BSE images of hibonite crystals (dark) in melt of CAI composition

634 produced by equilibrating (a) (0.15, 1.0) in melt A at IW-4.3 and (c) (0.15, 1.0) in melt B at

635 IW-3.3. (b) Ti, Ca, and Al composite elemental map, highlighting the distribution of Ti in a

636 crystal of hibonite, of the area indicated by the box in (a). Elemental maps corresponding to

637 the area indicated by the box in (c) are shown for (d) Al, (e) Ti, and (f) Mg. The scale bars in

638 (a) and (c) are 20 μm and those in (b) and (d) are 2 μm.

639

640 Figure 4: Variations of SiO_2 (circles) and MgO (squares) determined by EPMA as a function

641 of distance from the edge to centre of a crystal of hibonite in glass for sample (0.30, 1.0)

642 equilibrated with melt A at IW-2.3. The values at Position = 5 μm are reported in Table 2.

643

644 Figure 5: (a) c lattice parameter of hibonite and (b) wt% hibonite determined by QPA of

645 samples obtained by equilibrating oxides corresponding to the hibonite compositions (0.98,

646 0.0) (open squares), (0.62, 0.6) (solid circles) and (0.33, 1.0) (open circles) at 1400 ˚C and

647 various values of log$f$O$_2$ relative to the IW buffer. Error bars are smaller than the symbols.

648

649 Figure 6: Ti K-edge XANES spectra of natural hibonite samples (a) 10-43 (0.55 Ti pfu) and

650 (c) 7-981 (0.1 Ti pfu) from the Murchison carbonaceous chondrite, and synthetic hibonite

651 with compositions (b) (0.44, 0.0) and (d) (0.1, 0.0). Spectra are offset for clarity.

652

653 Figure 7: The pre-edge region of Ti K-edge XANES spectra of natural hibonite samples (a)

654 10-43 (0.55 Ti pfu) and (b) 7-981 (0.1 Ti pfu) from the Murchison carbonaceous chondrite,

655 and synthetic hibonite with compositions (c) (0.1, 0.0), (d) (0.2, 0.0), (e) (0.3, 0.0), (f) (0.44,

656 0.0), (g) (0.98, 0.0), and (h) (0.2, 1.0). Spectra are offset for clarity.

657

658 Figure 8: Simulated Ti K-edge XANES spectra of hibonite, modelled using FDMNES, with

659   (a) Ti^{4+} on M2, (b) Ti^{4+} on M4, (c) Ti^{4+} clustered on adjacent M4, (d) Ti^{4+} on M2 (20%) and

660   Ti^{4+} clustered on adjacent M4 (80%), (e) Ti^{3+} on M2, and (f) Ti^{3+} clustered on adjacent M4.

661   Spectra are offset for clarity.

662

663   Figure 9: The pre-edge region of the Ti K-edge XANES spectrum of (a) natural hibonite

664   sample 10-43, and simulated spectra, modelled using FDMNES, of hibonite with (b) Ti^{4+} on

665   M2 (20%) and Ti^{4+} clustered on adjacent M4 (80%), (c) Ti^{4+} clustered on adjacent M4, (d)

666   Ti^{4+} on M4, and (e) Ti^{4+} on M2. Spectra are offset for clarity.

667

668   Figure 10: Correlation between Mg and Ti + Si pfu for hibonite crystals equilibrated in a CAI

669   composition melt at 1450 ˚C and the values of fO_2, in log units relative to the IW buffer,

670   indicated. The line is the best fit to the data and has a slope of ~ 0.8.

20

Table 1: Lattice parameters and Mg and Ti site occupancies (as fractions of 1) of synthetic hibonite with $Ti^{3+}/\Sigma Ti = 0$ determined by Rietveld refinement of XRD data. Ti^{4+} (M4) was calculated assuming that Ti^{4+} pfu = Mg^{2+} pfu.

Sample	a (Å)	c (Å)	Volume (Å^3)	Mg (M3)	Ti^{4+} (M2*)	Ti^{4+} (M4)	Ti^{4+} (M2/M4)
(0.0, 0.0)	5.55769(2)	21.8958(2)	585.708(4)	-	-	-	-
(0.10, 0.0)	5.56305(2)	21.9095(1)	587.204(3)	0.05	0.035(5)	0.015(5)	2.33(84)
(0.20, 0.0)	5.56790(2)	21.92436(9)	588.627(3)	0.10	0.050(5)	0.050(5)	1.00(14)
(0.30, 0.0)	5.57443(2)	21.9430(1)	590.512(3)	0.15	0.065(5)	0.085(5)	0.76(7)
(0.40, 0.0)	5.58060(2)	21.9653(1)	592.419(3)	0.20	0.075(5)	0.125(5)	0.60(5)
(0.44, 0.0)	5.58874(7)	21.9986(6)	595.05(1)	0.21	0.05(1)	0.16(2)	0.31(7)
(0.98, 0.0)	5.6065(1)	22.0700(5)	600.79(3)	0.48	0.136(7)	0.34(1)	0.40(2)

*Site is half occupied.

Table 2: Compositions of hibonite crystals, expressed as wt% oxide and cations per formula unit for 19 oxygens, after equilibration of $CaAl_{12-y}Ti^{3+}_yO_{19}$ ($Ti^{3+}/\Sigma Ti = 1$) hibonite with melt composition A or B at various values of $\log fO_2$ relative to the IW buffer. $Ti^{3+}/\Sigma Ti$ was calculated from stoichiometry assuming $Ti^{4+} = Mg$ and $Ti^{4+} + Si = Mg$. For some experiments two different hibonite compositions were identified.

Hibonite	Melt	ΔIW	CaO	Al_2O_3	MgO	TiO_2	SiO_2	Total	Ca	Al	Mg	Ti	Si	Total	$Ti^{3+}/\Sigma Ti$ $Ti^{4+}=Mg$	$Ti^{3+}/\Sigma Ti$ $Ti^{4+}+Si=Mg$
					wt % (±0.02)						pfu (±0.01)					
(0.30, 1.0)	A	-0.3	9.45	82.98	1.66	3.60	0.96	98.64	1.15	11.15	0.28	0.31	0.11	13.01	0.09(5)	0.44(6)
(0.30, 1.0)	A	-1.3	8.69	84.15	1.80	3.72	0.34	98.71	1.06	11.28	0.31	0.32	0.04	13.00	0.04(4)	0.16(5)
(0.30, 1.0)	B	-1.3	8.87	86.18	1.38	2.78	0.29	99.51	1.07	11.44	0.23	0.24	0.03	13.01	0.02(6)	0.15(7)
(0.30, 1.0)	A	-2.3	8.83	84.12	1.77	3.87	0.32	98.91	1.07	11.26	0.30	0.33	0.04	13.00	0.09(4)	0.20(5)
(0.25, 1.0)	B	-2.3	9.06	87.17	0.65	1.03	0.54	98.46	1.10	11.66	0.11	0.09	0.06	13.02	0.00(16)	0.45(20)
(0.15, 1.0)	A	-3.3	9.20	85.78	1.34	2.80	0.46	99.58	1.11	11.39	0.23	0.24	0.05	13.02	0.05(6)	0.27(7)
(0.15, 1.0)	A	-3.3	9.02	85.46	1.50	3.36	0.47	99.82	1.09	11.33	0.25	0.28	0.05	13.00	0.12(5)	0.30(6)
(0.15, 1.0)	B	-3.3	8.93	88.60	0.67	1.36	0.14	99.70	1.07	11.70	0.11	0.11	0.02	13.02	0.02(10)	0.16(15)
(0.15, 1.0)	B	-3.3	8.79	84.32	1.66	3.64	0.23	98.63	1.07	11.31	0.28	0.31	0.03	13.01	0.10(5)	0.18(5)
(0.30, 1.0)	A	-3.3	9.21	88.31	0.64	1.24	0.37	99.77	1.11	11.66	0.11	0.10	0.04	13.02	0.00(12)	0.37(17)
(0.30, 1.0)	A	-4.3	8.81	85.35	1.54	3.46	0.23	99.38	1.07	11.36	0.26	0.29	0.03	13.00	0.12(5)	0.21(6)
(0.15, 1.0)	A	-6.3	9.17	87.98	0.54	1.32	0.15	99.16	1.11	11.70	0.09	0.11	0.02	13.02	0.19(13)	0.34(15)
(0.15, 1.0)	A	-6.3	9.03	85.99	1.24	2.92	0.28	99.47	1.09	11.43	0.21	0.25	0.03	13.01	0.16(6)	0.29(7)
(0.15, 1.0)	B	-6.3	9.32	87.72	0.89	1.65	0.69	100.27	1.11	11.54	0.15	0.14	0.08	13.02	0.00(10)	0.49(13)
(0.25, 1.0)	A	-6.3	9.01	83.56	1.76	4.33	0.34	99.01	1.10	11.19	0.30	0.37	0.04	13.00	0.19(4)	0.30(5)
(0.25, 1.0)	A	-6.3	8.95	85.52	1.07	2.85	0.41	98.80	1.09	11.43	0.18	0.24	0.05	12.99	0.26(6)	0.45(7)

Table 3: Lattice parameters of hibonite and the proportion of phases (wt %), determined by Rietveld QPA refinement, obtained after equilibrating three hibonite compositions at 1400 ˚C and various values of $\log fO_2$ relative to the IW buffer.

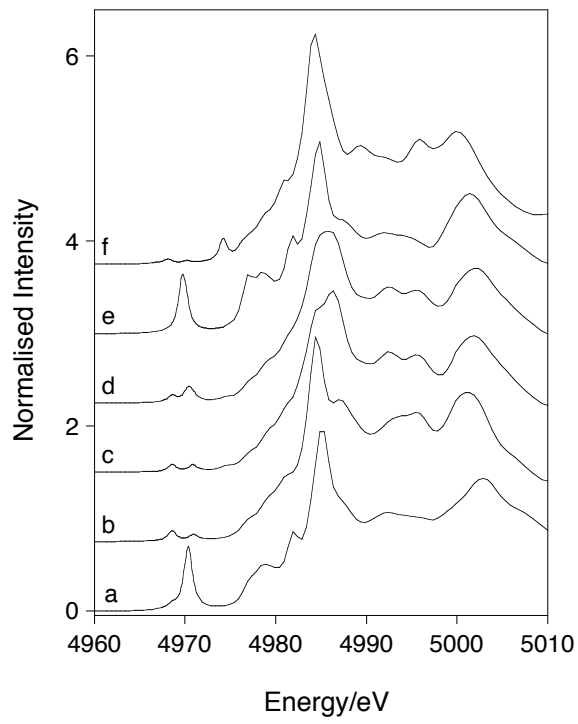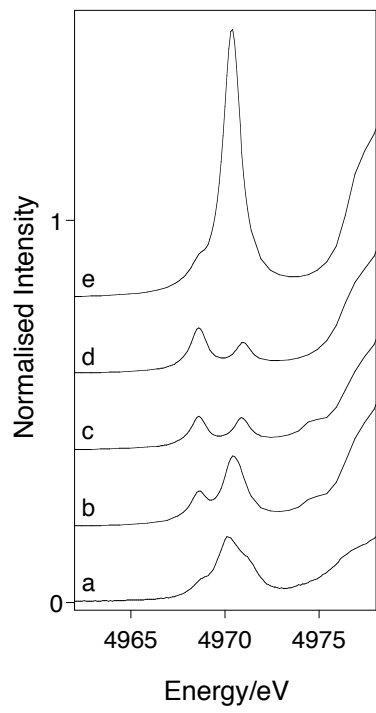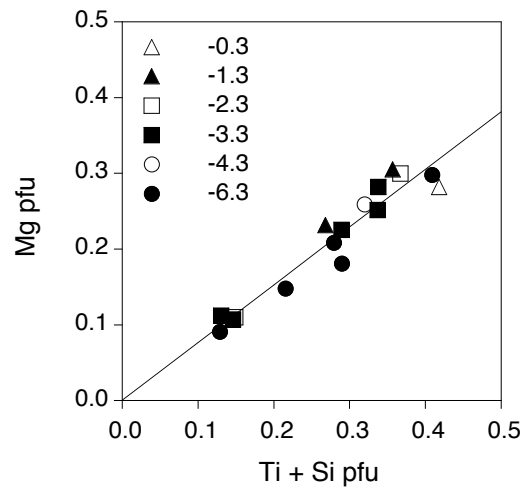| Composition	ΔIW	a (Å)	c (Å)	Volume (Å^3)	hibonite	CaTiO$_3$	MgAl$_2$O$_4$	Al$_2$O$_3$	Al$_2$TiO$_5$	TiO	TiO$_2$
(0.33, 1.0)											
	-6.3	5.56676(6)	21.9471(3)	589.00(2)	98.9(4)	-	-	-	-	1.1(1)	-
	-2.3	5.56448(5)	21.9363(4)	588.23(1)	61.5(3)	5.5(1)	-	32.0(2)	1.0(1)	-	-
	-0.3	5.56566(5)	21.9384(4)	588.53(1)	51.0(3)	6.0(1)	-	42.0(2)	1.0(1)	-	-
	2.3	5.56417(5)	21.9330(4)	588.07(1)	49.1(3)	6.3(1)	-	43.2(2)	1.4(1)	-	-
	4.3	5.56476(6)	21.9348(5)	588.24(1)	48.2(3)	6.2(1)	-	43.9(2)	1.7(1)	-	-
	7.3	5.56472(5)	21.9345(4)	588.23(1)	51.0(3)	6.3(1)	-	41.3(2)	1.4(1)	-	-
(0.62, 0.6)											
	-6.3	5.57720(4)	21.9850(3)	592.23(1)	93.8(4)	0.9(1)	-	4.9(1)	-	0.4(1)	-
	-2.3	5.57725(3)	21.9686(3)	591.80(1)	97.0(3)	3.0(1)	-	-	-	-	-
	-0.3	5.57634(3)	21.9609(3)	591.40(1)	95.5(4)	0.6(1)	-	-	3.9(1)	-	-
	2.3	5.57527(3)	21.9614(3)	591.18(1)	97.1(3)	-	-	-	2.9(1)	-	-
	4.3	5.57470(3)	21.9561(2)	590.92(1)	95.7(3)	-	-	-	4.3(1)	-	-
	7.3	5.57511(3)	21.9616(3)	591.15(1)	97.9(3)	-	-	-	2.1(1)	-	-
(0.98, 0.0)											
	-6.3	5.60052(8)	22.0532(7)	599.04(4)	87.1(4)	3.1(1)	8.8 (1)	-	-	-	1.0(1)
	-2.3	5.60843(6)	22.0745(5)	601.32(1)	93.0(4)	2.1(1)	4.5 (1)	0.4(1)	-	-	-
	2.3	5.60949(4)	22.0843(4)	601.81(1)	96.1(4)	1.4(1)	2.0 (1)	-	0.5(1)	-	-
	4.3	5.60959(3)	22.0843(5)	601.83(1)	97.2(3)	1.1(1)	1.7 (1)	-	-	-	-
	7.3	5.60886(4)	22.0856(4)	601.71(1)	96.0(3)	1.7(1)	2.3 (1)	-	-	-	-
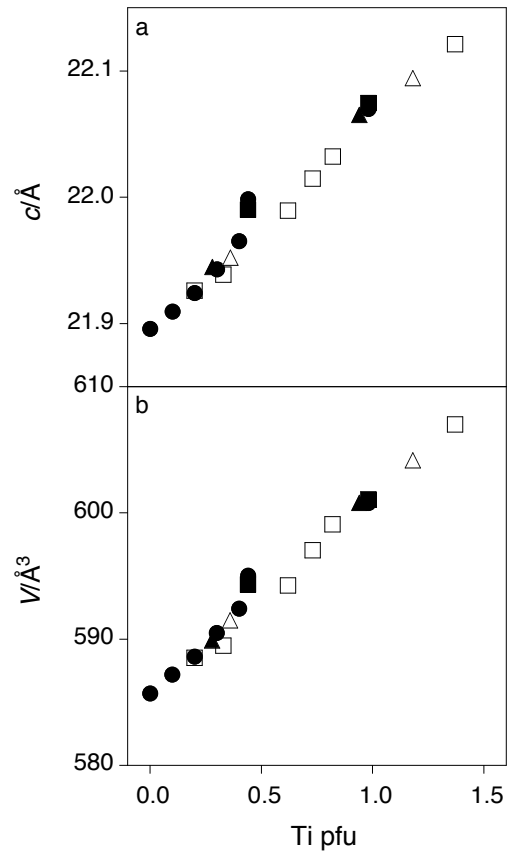
Figure 1
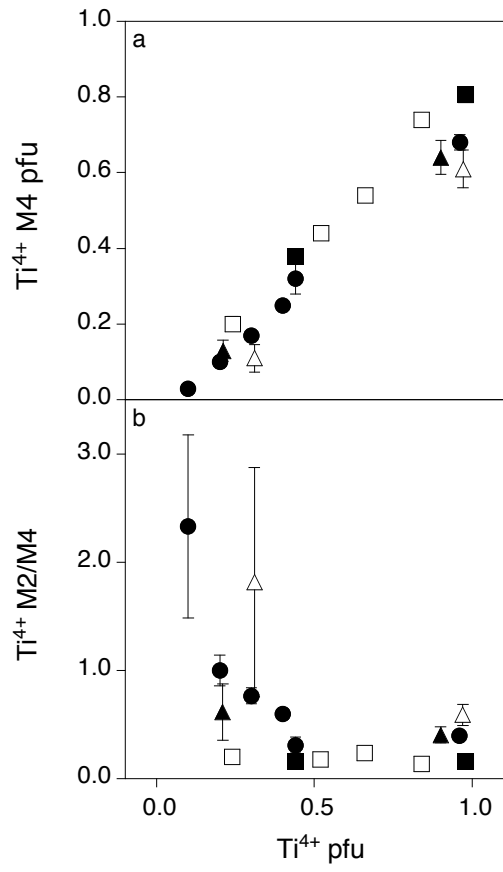
Figure 2
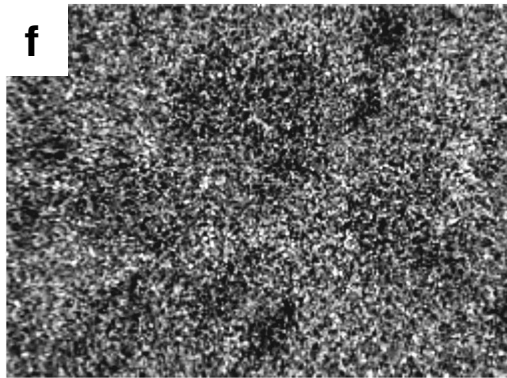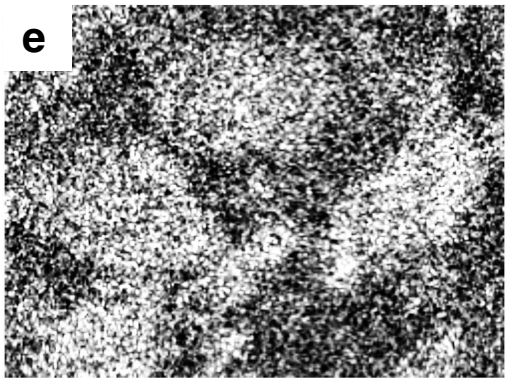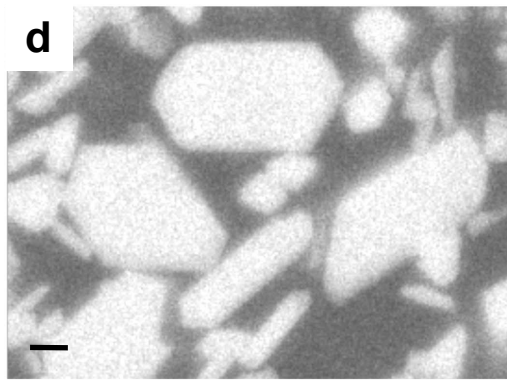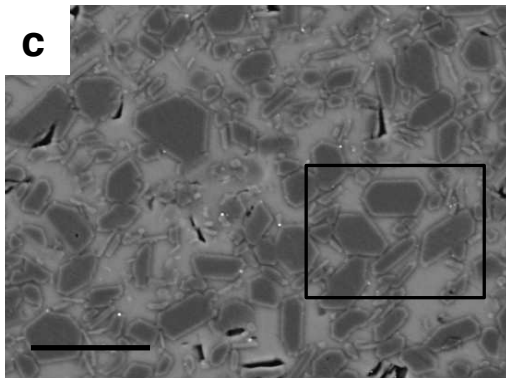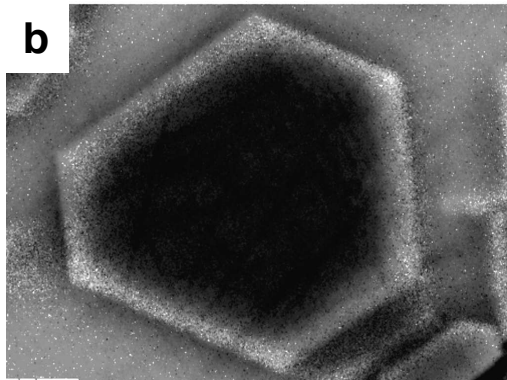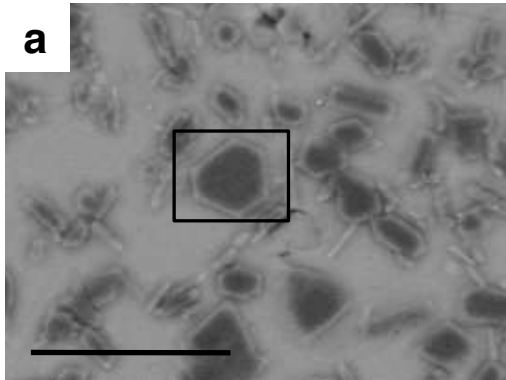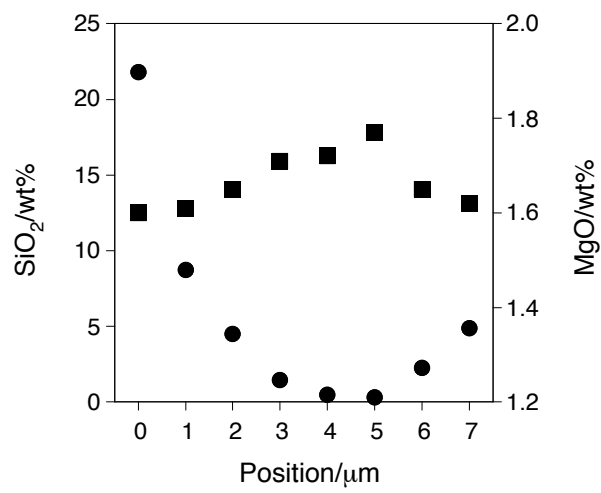
Figure 4
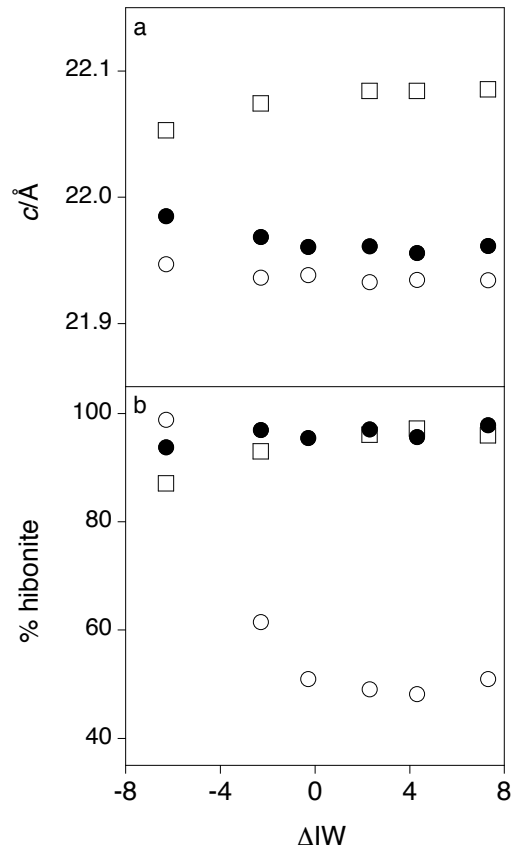
Figure 5
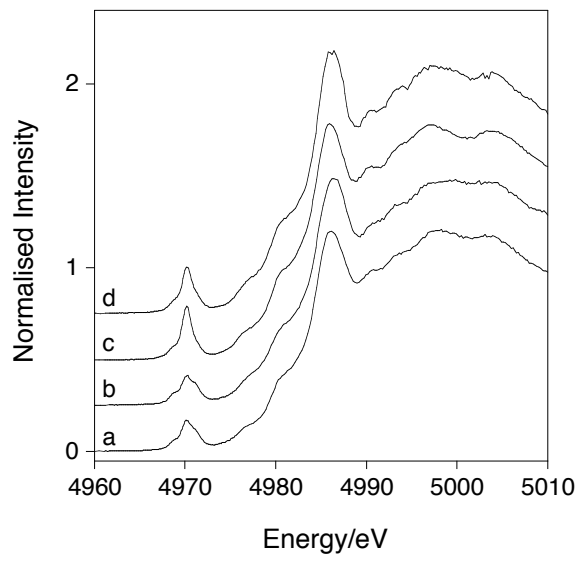
Figure 6
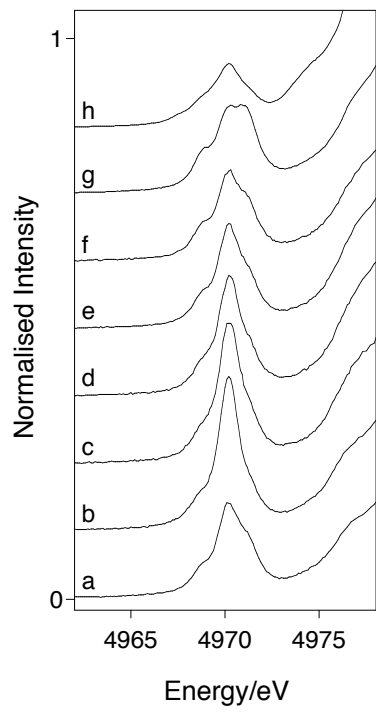
Figure 7

Figure 8

Figure 9

Figure 10